INTERNATIONAL JOURNAL FOR NUMERICAL METHODS IN FLUIDS, VOL. 18, 449–469 (1994)

A NUMERICAL METHOD FOR 3D VISCOUS INCOMPRESSIBLE FLOWS USING NON-ORTHOGONAL GRIDS

P. HE

Institute of Applied Mathematics, The University of British Columbia, Vancouver, B.C. V6T 1Z2, Canada

AND

M. SALCUDEAN

Department of Mechanical Engineering, The University of British Columbia, Vancouver, B.C. V6T 1Z4, Canada

SUMMARY

This paper presents a numerical method for fluid flow in complex three-dimensional geometries using a body-fitted co-ordinate system. A new second-order-accurate scheme for the cross-derivative terms is proposed to describe the non-orthogonal components, allowing parts of these terms to be treated implicitly without increasing the number of computational molecules. The physical tangential velocity components resulting from the velocity expansion in the unit tangent vector basis are used as dependent variables in the momentum equations. A coupled equation solver is used in place of the complicated pressure correction equation associated with grid non-orthogonality. The co-ordinate-invariant conservation equations and the physical geometric quantities of control cells are used directly to formulate the numerical scheme, without reference to the co-ordinate derivatives of transformation. Several two- and three-dimensional laminar flows are computed and compared with other numerical, experimental and analytical results to validate the solution method. Good agreement is obtained in all cases.

KEY WORDS Body-fitted co-ordinates Non-orthogonal grids Physical geometric quantities Incompressible flow Coupled equation solver

1. INTRODUCTION

Considerable progress has been made in recent years in the application of computational fluid dynamics to engineering problems. Efficient methods have been developed to compute fluid flow and heat transfer in problems with regular geometries where the domain boundaries fall along the lines of an analytic orthogonal co-ordinate system. However, many practical problems require geometrically complex computational domains. One such example is the film cooling of turbine blades.[1] In order to simulate this complex cooling process, the computational region should include not only the curved turbine blade surface but also the cooling orifices within the blade.

For problems with complex geometries, finite element methods appear to be the natural choice owing to their intrinsic geometric flexibility. Finite volume/difference methods, however, are well established in computational fluid dynamics and an alternative approach would be to use these methods with an appropriate body-fitted co-ordinate system.[3–13] Such methods can be developed on the basis of well-established solution algorithms and numerical codes for the regular geometries.

CCC 0271-2091/94/050449-21

Received 3 December 1992
Revised 27 August 1993

Curvilinear co-ordinates with orthogonal and non-orthogonal grids have been extensively used for fluid flow in complex geometries. The governing equations are considerably simpler in orthogonal co-ordinates; however, these methods have serious geometric limitations. Orthogonal grids are difficult to generate, especially in three dimensions. For complex three-dimensional domains, non-orthogonal grids are often necessary because they provide greater flexibility in the distribution of the grid points.

The use of a curvilinear co-ordinate system can entail a number of difficulties which have to be addressed. Some of these are described in the following. Most grid generation techniques provide discrete grid points rather than the analytic functions of transformation. In such cases the co-ordinate derivatives of transformation or the covariant base vectors $\mathbf{a}_i = (\partial x/\partial \xi_i, \partial y/\partial \xi_i, \partial z/\partial \xi_i)$ are usually computed approximately and other metric quantities such as contravariant base vectors and the Jacobian determinant are then evaluated from these co-ordinate derivatives. The definition and calculation of these derivatives, however, become ambiguous when a non-smooth grid is used. The procedure used to approximate these quantities is critical and may lead to significant numerical errors or even unrealistic solutions.[12]

Secondly, significant deterioration of the convergence rate of some of the available iterative solution procedures can occur with a non-orthogonal grid,[13,14] especially when the grid is highly non-orthogonal. This is partially due to the explicit treatment of the large non-orthogonal diffusion terms, which can be described analytically by cross-derivative terms such as $(\partial/\partial \xi_2)(\Gamma g^{12} \partial u/\partial \xi_1)$ and $(\partial/\partial \xi_3)(\Gamma g^{13} \partial u/\partial \xi_1)$ in the momentum equations.

The choice of dependent variables in the momentum equations also requires careful consideration. When Cartesian velocity components are used as dependent variables,[3-5,13] the conservation of momentum is considered along fixed directions everywhere in the field and no curvature terms appear in the momentum equations. The applicability and performance of the scheme, however, depend on the orientation of the computational grid relative to the reference Cartesian co-ordinate system. In the staggered approach, zero convective fluxes across the control volume faces may occur when the grid turns by 90° and one Cartesian velocity component is stored on each cell face. Grid-oriented velocities can be used as dependent variables[7-11] in order to eliminate this difficulty. The use of grid-oriented velocity components, however, leads to grid-sensitive curvature terms in the momentum equations. Such terms depend on the second derivative of grid co-ordinates and thus are difficult to discretize in a conservative manner, possibly leading to severe inaccuracies.[5,8]

Most of the work reported in the current literature uses a variant of the SIMPLE algorithm[2] to couple the pressure and velocity fields. The extension of this technique to non-orthogonal grids results in a very complex pressure correction equation, especially for three-dimensional cases.[13]

The present study proposes a method for the computation of flows in complex geometries that attempts to solve some of the problems described above. The method addresses the requirements of simulating complex three-dimensional problems such as the film cooling of turbine blades.[1] Efforts are made to achieve greater flexibility in grid design using significantly non-orthogonal and moderately non-smooth grids. To solve the problem related to the non-orthogonal grid, a new second-order-accurate numerical scheme is proposed to describe the cross-derivative terms. This scheme allows implicit treatment for part of the non-orthogonal terms without increasing the size of the computational molecules. To avoid inaccurate discretization for a non-smooth grid, the physical geometric quantities (volumes, surface area vectors, etc.) are calculated directly and used to formulate the numerical schemes. These geometric quantities are calculated in such a way as to satisfy the geometric conservation laws described by Vinokur.[15] When the divergence theorem is used over a control cell, the conservation equation can be expressed accurately for an arbitrary grid using these geometric quantities. Such an

approach yields an overall convervative approximation for any grid and provides a better physical understanding of the resulting formulation.

The proposed method uses the physical tangential velocity components as dependent variables in the momentum equations. These variables are the contravariant velocity unknowns and the volume flow rates across cell faces with appropriate normalization. Similarly to other grid-oriented velocity unknowns, the choice of such dependent variables gives rise to additional curvature terms. These terms can be expressed by Christoffel symbols using tensor notation[8] and discretized directly.[7,8] In the present study a different approach is followed which avoids the explicit discretization of the second-order co-ordinate derivatives. A coupled equation solver combined with a staggered grid approach is used to solve the momentum and continuity equations directly, eliminating the need for a complex pressure correction equation.

The proposed method is described by first presenting the derivation of the discretized general governing equation and the numerical scheme for the non-orthogonal terms. This scheme is then proven to be second-order-accurate. Next, the treatment of the momentum equations and curvature terms using the tangential velocity components as the dependent variables is described, followed by a description of the overall coupled solution procedure in the curvilinear co-ordinate system. Finally, four computational examples are presented to demonstrate the capabilities of the method.

2. NUMERICAL FORMULATION

This section describes the discretization of a general scalar governing equation which forms the basis for the discretization of the momentum equations. The geometric quantities used in our discretization are described first. The divergence theorem is then used to integrate the governing equation. Finally, the new discretization method for the non-orthogonal terms is described and the second-order accuracy is proven.

2.1. Geometric quantities

The physical geometric quantities for the control cells are used directly. A uniform grid with mesh size $\Delta\xi_i = 1$ is assumed in the transformed computational domain.

The geometric quantities used in the present study are illustrated in Figure 1. The unit tangent vectors $\mathbf{e}_i$ $(i = 1, 2, 3)$ are calculated at the centres of the control volume surfaces and are

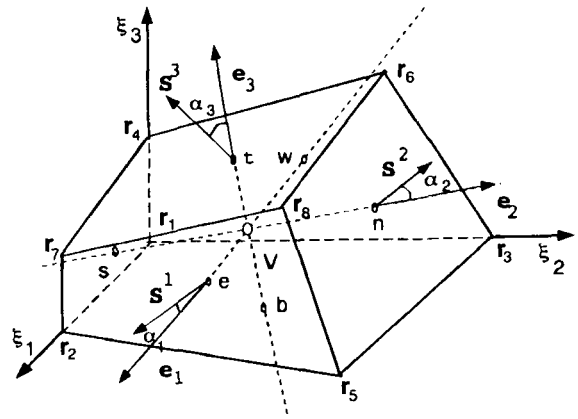

Figure 1. Illustration of the physical geometric quantities for a control cell

locally parallel to the co-ordinate lines ξ_i. These tangent vectors correspond to the normalized covariant base vectors $\mathbf{a}_i$ in the literature. The surface area vectors $\mathbf{S}^i$ ($i = 1, 2, 3$) are also defined at the same points as $\mathbf{e}_i$ and are normal to the control volume surfaces, with magnitude $|\mathbf{S}^i|$ equal to the corresponding surface area. The volume of the control cell is denoted by V.

The quantities $\mathbf{e}_i$, $\mathbf{S}^i$ and V are the basic grid quantities and are calculated directly using discrete grid points. For convenience of formulation, two additional quantities are defined from the above geometric quantities. The non-orthogonal angles α_i are defined as the angles between the surface area vectors $\mathbf{S}^i$ and the tangential vectors $\mathbf{e}_i$. These angles are a measure of the degree of grid non-orthogonality; for an orthogonal grid these angles are zero. The surface area vectors $\mathbf{S}^i$ are rescaled and denoted as $\mathbf{e}^i = \mathbf{S}^i/|\mathbf{S}^i| \cos \alpha_i$.

2.2. *Calculation of the geometric quantities*

In general, the geometric quantities have to be evaluated from discrete grid points. The unit tangent vectors $\mathbf{e}_i$ are calculated by second-order-accurate averaging (using the centre points of two neighbouring control cells).

The faces of a control cell are generally surfaces rather than planes, as illustrated in Figure 2. In fact, it is not always possible to fit a plane through four points. The surface area vectors and volume of a control cell can be approximated directly by various formulae.

To approximate the surface area vectors and volume of a cell, the following formulae for a triangle and a pyramid are used. A properly oriented surface area vector for a triangular face with vertices $\mathbf{r}_1$, $\mathbf{r}_2$ and $\mathbf{r}_3$, is given by

$$(\mathbf{r}_2 - \mathbf{r}_1) \times (\mathbf{r}_3 - \mathbf{r}_1)/2, \tag{1}$$

while the volume for a pyramid with vertices $\mathbf{r}_1$, $\mathbf{r}_2$, $\mathbf{r}_3$ and $\mathbf{r}_4$ is given by

$$\tfrac{1}{6}[(\mathbf{r}_2 - \mathbf{r}_1) \times (\mathbf{r}_3 - \mathbf{r}_1)] \cdot (\mathbf{r}_4 - \mathbf{r}_1) = \tfrac{1}{3}\mathbf{S} \cdot (\mathbf{r}_4 - \mathbf{r}_1). \tag{2}$$

Using equations (1) and (2), we can employ various averaging processes to calculate the geometric quantities for an arbitrary cell with straight line edges. Each polygonal face is divided into plane triangular faces and the total volume is treated as a sum of tetrahedra. In order to obtain an accurate discretization, the geometric quantities are calculated according to the geometric

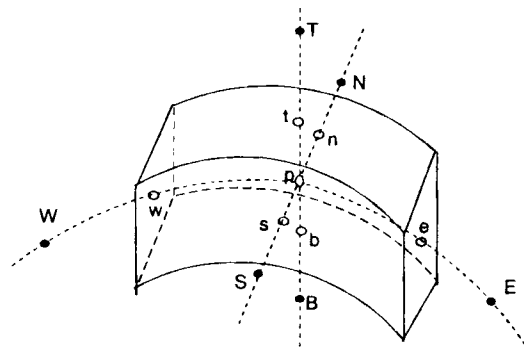

Figure 2. A general control volume. Nodes to the north, south, east, west, top and bottom are represented by N, S, E, W, T and B respectively. Lowercase letters denote control volume surfaces

conservation laws described in Reference 15 and the following formulae for surface area vectors and volume are used:

$$\mathbf{S}_{\mathrm{w}}^{1} = (\mathbf{r}_6 - \mathbf{r}_1) \times (\mathbf{r}_3 - \mathbf{r}_4)/2, \tag{3}$$

$$V = \tfrac{1}{3}(\mathbf{S}_{\mathrm{w}}^{1} + \mathbf{S}_{\mathrm{s}}^{2} + \mathbf{S}_{\mathrm{b}}^{3}) \cdot (\mathbf{r}_8 - \mathbf{r}_1), \tag{4}$$

where the subscripts 'w' 's' and 'b' indicate locations west, south and bottom respectively (Figure 1) of the vectors. From the two basic vectors $\mathbf{S}$ and $\mathbf{e}_i$ the quantities $\cos \alpha_i$ and $\mathbf{e}^i$ can be calculated.

Noting that $\mathbf{r}_2 - \mathbf{r}_1$, $\mathbf{r}_3 - \mathbf{r}_1$ and $\mathbf{r}_4 - \mathbf{r}_1$ are approximations of the covariant vectors $\mathbf{a}_1 = \partial \mathbf{r}/\partial \xi_1$, $\mathbf{a}_2 = \partial \mathbf{r}/\partial \xi_2$ and $\mathbf{a}_3 = \partial \mathbf{r}/\partial \xi_1$ respectively, we can see that $\mathbf{S}^1 \approx \mathbf{a}_2 \times \mathbf{a}_3$ and $V \approx (\mathbf{a}_1 \times \mathbf{a}_2) \cdot \mathbf{a}_3$ from formulae (1) and (2). Since the volume element $\sqrt{g}$ and the contravariant vectors $\mathbf{a}^i$ satisfy $\sqrt{g} = (\mathbf{a}_1 \times \mathbf{a}_2) \cdot \mathbf{a}_3$ and $\mathbf{a}^1 = (\mathbf{a}_2 \times \mathbf{a}_3)/\sqrt{g}$ respectively,[16] we have $\mathbf{S}^1 \approx \sqrt{g}\mathbf{a}^1$ and $V \approx \sqrt{g}$. The volume element $\sqrt{g}$ is the inverse of the Jacobian determinant.

The geometric quantities at the positions described in Section 2.1 are calculated from known discrete points. For other locations the values for $\mathbf{e}^i$ and V are computed by a second-order-accurate interpolation and the unit tangent vectors are calculated from $\mathbf{e}^i$ by orthogonal relations $\mathbf{e}^i \cdot \mathbf{e}_j = 0$ $(i \neq j)$ instead from $\mathbf{e}_i$ by averaging.

2.3. Discretization

The general transport equation for a dependent variable ϕ is written as

$$\nabla \cdot (\rho \mathbf{u} \phi) - \nabla \cdot (\Gamma \nabla \phi) + C = 0, \tag{5}$$

where $\mathbf{u}$, ρ and Γ are the velocity, density and diffusion coefficient respectively. The first term represents transport of ϕ by convection and the second term represents transport by molecular diffusion. The last term C is a source term which generally depends on ϕ. This equation is the natural expression of the transport of ϕ and takes different forms in various co-ordinate systems. The discretized equations were obtained by first integrating equation (5) over a control volume in the physical space and then deriving an algebraic approximation to this integral equation. Geometric quantities associated with the control volume are used directly to evaluate the fluxes on the control cell surfaces.

Let $\mathbf{J} = \rho \mathbf{u} \phi - \Gamma \nabla \phi$ denote the total flux. Equation (5) can then be written as

$$\nabla \cdot \mathbf{J} + C = 0. \tag{6}$$

Equation (6) is integrated over a general control volume δV, as shown in Figure 2 in the physical space, and the divergence theorem is applied:

$$\iiint_{\delta V} \nabla \cdot \mathbf{J} \, \mathrm{d}v = \oint_{\partial V} \mathbf{J} \cdot \mathrm{d}\mathbf{S} \approx \mathbf{J} \cdot \mathbf{S}^1|_{\mathrm{e}} - \mathbf{J} \cdot \mathbf{S}^1|_{\mathrm{w}} + \mathbf{J} \cdot \mathbf{S}^2|_{\mathrm{n}} - \mathbf{J} \cdot \mathbf{S}^2|_{\mathrm{s}} + \mathbf{J} \cdot \mathbf{S}^3|_{\mathrm{t}} - \mathbf{J} \cdot \mathbf{S}^3|_{\mathrm{b}}. \tag{7}$$

Next consider the transport of ϕ along the ξ_i-co-ordinate direction:

$$\mathbf{J} \cdot \mathbf{S}^i = \rho \phi \mathbf{u} \cdot \mathbf{S}^i - \Gamma \nabla \phi \cdot \mathbf{S}^i = \rho \phi F^i - \Gamma \nabla \phi \cdot \mathbf{S}^i, \tag{8}$$

where

$$F^i = \mathbf{u} \cdot \mathbf{S}^i \quad (i = 1, 2, 3)$$

are the volume flow rates across the cell faces. By the definition of gradient,

$$\nabla\phi = \left(\oint_S \phi \, d\mathbf{S}\right) \Big/ V.$$

Applying the Gauss divergence theorem, we obtain

$$(\nabla\phi)_P = [\mathbf{S}^1(\phi_e - \phi_w) + \mathbf{S}^2(\phi_n - \phi_s) + \mathbf{S}^3(\phi_t - \phi_b)]/V, \tag{9}$$

where $\phi_e - \phi_w$, $\phi_n - \phi_s$ and $\phi_t - \phi_b$ are approximations of $\partial\phi/\partial\xi_1$, $\partial\phi/\partial\xi_2$ and $\partial\phi/\partial\xi_3$ respectively, since $\Delta\xi_i = 1$ in the transformed space. Hence the gradient of the dependent variable ϕ can be expressed as

$$\nabla\phi = \frac{1}{V}\left(\mathbf{S}^1 \frac{\partial\phi}{\partial\xi_1} + \mathbf{S}^2 \frac{\partial\phi}{\partial\xi_2} + \mathbf{S}^3 \frac{\partial\phi}{\partial\xi_3}\right). \tag{10}$$

Substituting equation (10) into (8), we obtain the following expression for the transport of ϕ:

$$\mathbf{J}\cdot\mathbf{S}^i = \rho\phi F^i - \Gamma g^{ii} \frac{\partial\phi}{\partial\xi_i} - \sum_{i\neq j} \Gamma g^{ij} \frac{\partial\phi}{\partial\xi_j}, \tag{11}$$

where

$$g^{ij} = \frac{\mathbf{S}^i \cdot \mathbf{S}^j}{V} \quad (i, j = 1, 2, 3)$$

is the surface area metric tensor. When the grid is orthogonal, $g^{ij} = 0$ for $i \neq j$; therefore the last term in (11) is the result of grid non-orthogonality. The total transport of ϕ can be decomposed into an orthogonal component and a non-orthogonal component:

$$\mathbf{J}\cdot\mathbf{S}^i = J^i_O + J^i_N \quad (i = 1, 2, 3), \tag{12}$$

where

$$J^i_O = \rho\phi F^i - \Gamma g^{ii} \frac{\partial\phi}{\partial\xi_i}, \qquad J^i_N = -\sum_{i\neq j} \Gamma g^{ij} \frac{\partial\phi}{\partial\xi_j}.$$

Substituting equation (12) into (7), the conservation equation over the control cell can be written as

$$(J^1_O + J^1_N)|_e - (J^1_O + J^1_N)|_w + (J^2_O + J^2_N)|_n - (J^2_O + J^2_N)|_s + (J^3_O + J^3_N)|_t - (J^3_O + J^3_N)|_b + VC = 0. \tag{13}$$

The orthogonal component J^i_O has the same form as for the Cartesian co-ordinate system. Therefore schemes such as the hybrid scheme or the power law scheme[2] for regular geometries can be applied to these terms. The non-orthogonal components, however, cause some numerical difficulties. Ordinary discretization of the non-orthogonal terms, involving only the corner points, results in a 19-diagonal coefficient matrix which is not unconditionally diagonally dominant. This may result in numerical instability and unrealistic solutions. Direct solution methods are impractical for this 19-diagonal coefficient matrix.[14] Hence the common practice is to treat the non-orthogonal components of the equation explicitly, by combining them into the source term. This may cause serious deterioration in the convergence rate if these explicit components become

large. It is therefore necessary to investigate other treatments. In the present study a new numerical scheme is proposed to address this difficulty and is presented in the following subsection.

2.4. *Discretization of the non-orthogonal terms*

Referring to Figure 3, consider the approximation of one of the non-orthogonal terms, $g^{12}\Gamma\,\partial\phi/\partial\xi_2$, at the midpoint of the east surface. When the central difference scheme is used, there is no contribution to the main diagonal terms of the resulting coefficient matrix. Also, four additional corner points are involved, with at least two negative coefficients in the resulting discretization for the cross-derivative term $(\partial/\partial\xi_1)(g^{12}\,\partial\phi/\partial\xi_2)$, making an implicit treatment difficult. The following alternative approximation was introduced to solve this problem: if $g^{12}|_e \le 0$, then

$$\left.\frac{\partial\phi}{\partial\xi_2}\right|_e = \frac{\phi_{NE} - \phi_E + \phi_P - \phi_S}{2h}; \tag{14}$$

if $g^{12}|_e > 0$, then

$$\left.\frac{\partial\phi}{\partial\xi_2}\right|_e = \frac{\phi_N - \phi_P + \phi_E - \phi_{SE}}{2h}. \tag{15}$$

Different numerical schemes are chosen depending on the sign of the coefficient g^{12}, based on the preference for a positive contribution to the main diagonal term. The idea is similar to the upwind scheme for the convection terms, in which different expressions are employed for different signs of the velocity. In contrast with the one-side difference, this scheme is symmetrical around point 'e' and is second-order-accurate. This can be shown through the following order analysis.

With reference to Figure 3, the following are obtained using Taylor expansions:

$$\phi_{NE} - \phi_E = \left.\frac{\partial\phi}{\partial\xi_2}\right|_E h + \frac{1}{2}\left.\frac{\partial^2\phi}{\partial\xi_2^2}\right|_E h^2 + O(h^3), \qquad \phi_P - \phi_S = \left.\frac{\partial\phi}{\partial\xi_2}\right|_P h - \frac{1}{2}\left.\frac{\partial^2\phi}{\partial\xi_2^2}\right|_P h^2 + O(h^3).$$

Combining the above expressions yields

$$\phi_{NE} - \phi_E + \phi_P - \phi_S = \left(\left.\frac{\partial\phi}{\partial\xi_2}\right|_E + \left.\frac{\partial\phi}{\partial\xi_2}\right|_P\right)h + \frac{1}{2}\left(\left.\frac{\partial^2\phi}{\partial\xi_2^2}\right|_E - \left.\frac{\partial^2\phi}{\partial\xi_2^2}\right|_P\right)h^2 + O(h^3). \tag{16}$$

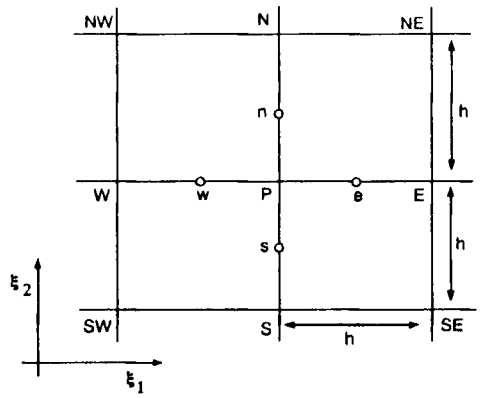

Figure 3. Illustration of discretization of cross-derivatives

Since

$$\left.\frac{\partial\phi}{\partial\xi_2}\right|_{\mathrm{E}} + \left.\frac{\partial\phi}{\partial\xi_2}\right|_{\mathrm{P}} = 2\left.\frac{\partial\phi}{\partial\xi_2}\right|_{\mathrm{e}} + \frac{1}{4}\frac{\partial^3\phi}{\partial\xi_1^2\partial\xi_2}h^2 + O(h^3), \tag{17}$$

$$\left.\frac{\partial^2\phi}{\partial\xi_2^2}\right|_{\mathrm{E}} - \left.\frac{\partial^2\phi}{\partial\xi_2^2}\right|_{\mathrm{P}} = \left.\frac{\partial^3\phi}{\partial\xi_1\partial\xi_2^2}\right|_{\mathrm{e}} h + O(h^2), \tag{18}$$

we can write equation (16) as

$$\left.\frac{\partial\phi}{\partial\xi_2}\right|_{\mathrm{e}} = \frac{\phi_{\mathrm{NE}} - \phi_{\mathrm{E}} + \phi_{\mathrm{P}} - \phi_{\mathrm{S}}}{2h} + O(h^2). \tag{19}$$

A similar estimate exists for approximation (15):

$$\left.\frac{\partial\phi}{\partial\xi_2}\right|_{\mathrm{e}} = \frac{\phi_{\mathrm{N}} - \phi_{\mathrm{P}} + \phi_{\mathrm{E}} - \phi_{\mathrm{SE}}}{2h} + O(h^2). \tag{20}$$

The above estimates show that the schemes (14) and (15) presented here are second-order-accurate. The other derivatives involved in the expressions for the non-orthogonal components can be treated similarly. This approach provides a second-order approximation for the non-orthogonal term $(\partial/\partial\xi_i)(g^{ij}\,\partial\phi/\partial\xi_j)$. Also, using this method, the number of corner points used is reduced by half and the main diagonal term of the resulting coefficient matrix, a_{P}, is augmented by the amount

$$2\Gamma(|g^{12}| + |g^{13}| + |g^{23}|).$$

After treating the non-orthogonal diffusion as described above, the general governing equation can be discretized following the methods developed for standard Cartesian co-ordinates. In the present study the power law scheme[2] is used for the orthogonal components.

A general algebraic equation is obtained by substituting the discretized forms of the orthogonal and non-orthogonal components into equation (13). The resulting equation can be written as

$$a_{\mathrm{P}}\phi_{\mathrm{P}} = a_{\mathrm{E}}\phi_{\mathrm{E}} + a_{\mathrm{W}}\phi_{\mathrm{W}} + a_{\mathrm{N}}\phi_{\mathrm{N}} + a_{\mathrm{S}}\phi_{\mathrm{S}} + a_{\mathrm{T}}\phi_{\mathrm{T}} + a_{\mathrm{B}}\phi_{\mathrm{B}} + \sum_{nc} a_{nc}\phi_{nc} + b \tag{21}$$

where a_{E}, a_{W}, etc. denote the combined convection–diffusion coefficients, including the non-orthogonal terms, the summation index nc represents the corner points from the discretization of non-orthogonal components of ϕ (such as ϕ_{WN} and ϕ_{WS}) and b includes only the source term C.

3. CALCULATION OF THE FLOW FIELD

The discretization of the momentum and continuity equations is presented in this section, along with an algebraic method for handling the curvature terms using the tangential velocity components as dependent unknowns.

3.1. Dependent variables in the momentum equations

Different sets of velocity unknowns may be chosen. A review of the various possibilities is given by Rodi *et al.*[5] In the present study the physical tangential velocity components are used as the dependent variables for the momentum equations. These variables, denoted as U^{ξ_i}, are the coefficients resulting from the velocity expansion in the unit tangent basis vectors $\mathbf{e}_i$:

$$\mathbf{u} = U^{\xi_1}\mathbf{e}_1 + U^{\xi_2}\mathbf{e}_2 + U^{\xi_3}\mathbf{e}_3. \tag{22}$$

An expansion in a two-dimensional tangential co-ordinate system is shown in Figure 4, where $OA_i = (\mathbf{S}/|\mathbf{S}|) \cdot \mathbf{u}$ are the physical contravariant velocity components and U^{ξ_i} are the physical tangential velocity components. The tangential velocity components U^{ξ_i} are uniquely determined by equation (22) and have the following expressions:[17]

$$U^{\xi_i} = \frac{\mathbf{S}^i \cdot \mathbf{u}}{|\mathbf{S}^i| \cos \alpha_i} = \mathbf{e}^i \cdot \mathbf{u}. \tag{23}$$

From the above equation it can be seen that the physical tangential velocity components are the volume flow rates $\mathbf{u} \cdot \mathbf{S}^i$ normalized by appropriate geometric quantities. The volume flow rates $\mathbf{u} \cdot \mathbf{S}^i$ were used as velocity unknowns by Rosenfeld *et al.*[7] and are equivalent to the quantities $\sqrt{g}U^i$. As reported by Segal *et al.*,[8] the use of the quantities $\sqrt{g}U^i$ as velocity unknowns provides a more accurate solution than the use of the contravariant velocities U^i.

The tangential velocity components are contravariant unknowns, equivalent to the quantities $\sqrt{g}U^i/|\mathbf{S}^i| \cos \alpha_i$. Unlike the contravariant velocities U^i, the U^{ξ_i} have the same magnitude as the actual velocity. This facilitates implementation of the boundary conditions.

Similarly to the use of the volume flow rates, the use of the tangential velocity components satisfies the velocity recovery requirement as described by Segal *et al.*[8] In fact, from the calculations of geometric quantities described in Section 2.2 and formulae (22) and (23), it is easy to see that the transformation $\mathbf{u} \rightarrow U^{\xi_i} \rightarrow \mathbf{v}$ gives exactly $\mathbf{v} = \mathbf{u}$ if $\mathbf{u}$ is a constant vector. Computational tests also show that the use of the tangential velocity components as velocity unknowns provides satisfactory performance.

3.2. Discretization of the momentum equations

A staggered grid arrangement is adopted in which the pressure is located at the geometric centre of the control volume and the tangential velocity components U^{ξ_i} lie at the midpoints of the respective control volume surfaces (see Figure 5). The use of the tangential velocity components as dependent variables gives rise to additional curvature terms, which can be expressed as Christoffel symbols using tensor notation. These terms can be discretized directly using e.g. central differencing.[7,8]

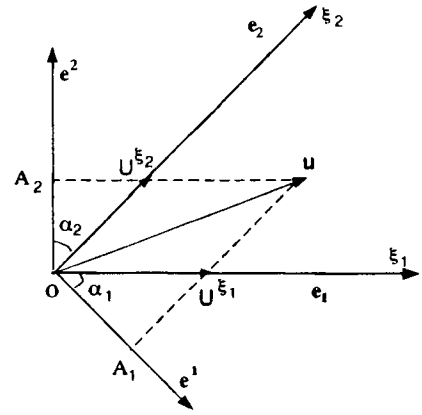

Figure 4. Illustration of the velocity expansion in a 2D local tangential vector basis velocity components as dependent unknowns.

Since these curvature terms involve second-order derivatives of the grid co-ordinates, they are difficult to discretize accurately when the grids become non-smooth. We avoid direct discretization of the curvature terms by an algebraic manipulation of the discretizations for the Cartesian velocity components. A similar approach was used in References 11 and 18, where the covariant velocities were used as dependent variables, with satisfactory results. This method seems more desirable for non-smooth grids, since the explicit discretization of second-order derivatives of the grid co-ordinates is avoided.

In order to discretize the momentum equations, auxiliary discretizations for the Cartesian velocity components are considered. Suppose that all three Cartesian velocity components are located at the U^{ξ_1}-position. The governing equations for the Cartesian velocity components can be taken as special cases of the general governing equation (5). The discretization for the Cartesian velocity components can be obtained according to the method outlined in the previous section. Since the Cartesian velocity components are assumed to share the same control cell as U^{ξ_1}, their discretization equations will have identical coefficients. Therefore the discretizations can be written in vector form as

$$a_{\mathrm{p}}^{\xi_1}\mathbf{u}_{\mathrm{p}} = a_{\mathrm{e}}^{\xi_1}\mathbf{u}_{\mathrm{e}} + a_{\mathrm{w}}^{\xi_1}\mathbf{u}_{\mathrm{w}} + a_{\mathrm{n}}^{\xi_1}\mathbf{u}_{\mathrm{n}} + a_{\mathrm{s}}^{\xi_1}\mathbf{u}_{\mathrm{s}} + a_{\mathrm{t}}^{\xi_1}\mathbf{u}_{\mathrm{t}} + a_{\mathrm{b}}^{\xi_1}\mathbf{u}_{\mathrm{b}} + \sum_{nc} a_{nc}^{\xi_1}\mathbf{u}_{nc} + \mathbf{b}^{\xi_1}, \tag{24}$$

where lowercase letters are used for the subscripts instead of uppercase to indicate that the U^{ξ_1} are located on cell faces instead of at cell centres. The source term $\mathbf{b}^{\xi_1}$ contains only the pressure gradient term, which is discretized by the central difference scheme. The above discretization for the momentum equations is co-ordinate-invariant and independent of the choice of dependent variables.

To find the discretization using the tangential velocity components as dependent variables, the velocity expansion in the local tangential vector basis at point 'p', $\{\mathbf{e}_i|_{\mathrm{p}}\}$, is considered. Taking the inner product of vector $\mathbf{e}_{\mathrm{p}}^1$ and vector equation (24) and applying formula (23), the following equation is obtained:

$$a_{\mathrm{p}}^{\xi_1}U_{\mathrm{p}}^{\xi_1} = \sum_{nb} a_{nb}^{\xi_1}(U_{nb}^{\xi_1})' + \sum_{nc} a_{nc}^{\xi_1}(U_{nc}^{\xi_1})' + (b^{\xi_1})', \tag{25}$$

where

$$(U_{nb}^{\xi_1})' = \mathbf{e}_{\mathrm{p}}^1 \cdot \mathbf{u}_{nb}, \qquad (U_{nc}^{\xi_1})' = \mathbf{e}_{\mathrm{p}}^1 \cdot \mathbf{u}_{nc}, \qquad (b^{\xi_1})' = \mathbf{e}_{\mathrm{p}}^1 \cdot \mathbf{b}^{\xi_1}, \tag{26}$$

the index *nb* represents the six nearest neighbours of the node 'p', namely 'e' (east), 'w' (west), 'n' (north), 's' (south), 't' (top) and 'b' (bottom), and the index *nc* represents the corner points as defined previously. The primed velocities $(U_{nb}^{\xi_1})'$ and $(U_{nc}^{\xi_1})'$ are velocity projections of neighbouring velocities over the vector $\mathbf{e}^1$ at point 'p'. The vector $\mathbf{e}^1$ changes from point to point in the flow field and therefore the velocities $(U_{nb}^{\xi_1})'$ generally differ from the actual neighbouring variables $U_{nb}^{\xi_1}$. Since the $(U_{nb}^{\xi_1})'$ are not dependent variables, they must be replaced by $U_{nb}^{\xi_1}$. This can be done by rearranging equation (25) as

$$a_{\mathrm{p}}^{\xi_1}U_{\mathrm{p}}^{\xi_1} = \sum_{nb} a_{nb}^{\xi_1}U_{nb}^{\xi_1} + \sum_{nc} a_{nc}^{\xi_1}U_{nc}^{\xi_1} + b^{\xi_1,\mathrm{c}} + b^{\xi_1}, \tag{27}$$

where

$$b^{\xi_1,\mathrm{c}} = \sum_{nb} a_{nb}^{\xi_1}[(U_{nb}^{\xi_1})' - U_{nb}^{\xi_1}] + \sum_{nc} a_{nc}^{\xi_1}[(U_{nc}^{\xi_1})' - U_{nc}^{\xi_1}]. \tag{28}$$

Equation (28) represents the curvature terms when the tangential velocity components are used as velocity unknowns. Using equations (23) and (26), equation (28) can be rewritten as

$$b^{\xi_1,c} = \sum_{nb} a_{nb}^{\xi_1}(\mathbf{e}_{nb}^1 - \mathbf{e}_p^1)\cdot\mathbf{u}_{nb} + \sum_{nc} a_{nc}^{\xi_1}(\mathbf{e}_{nc}^1 - \mathbf{e}_p^1)\cdot\mathbf{u}_{nc}. \tag{29}$$

The above equation shows that the curvature terms for U^{ξ_1} are produced by the change in vector $\mathbf{e}^1$ from point 'p' to neighbouring points.

For an actual computation the velocity $\mathbf{u}$ at neighbouring points is calculated from equation (22) and the curvature term $b^{\xi_1,c}$ is then calculated from equation (29). For a staggered grid the velocity unknowns U^{ξ_2} and U^{ξ_3} are not defined at the U^{ξ_1}-position and some interpolation is needed for the calculation of velocities $\mathbf{u}_{nb}$ and $\mathbf{u}_{nc}$.

The discretization equations for the other two velocity unknowns can be derived in a similar manner. The resulting discretization for the momentum equations, with part of the pressure difference term written explicitly, can be expressed as

$$a_w^{\xi_1}U_w^{\xi_1} = \sum_{nb} a_{nb}^{\xi_1}U_{nb}^{\xi_1} + \sum_{nc} a_{nc}^{\xi_1}U_{nc}^{\xi_1} + b^{\xi_1,c} + A_{\xi_1}(p_P - p_W) + b^{\xi_1}, \tag{30}$$

$$a_s^{\xi_2}U_s^{\xi_2} = \sum_{nb} a_{nb}^{\xi_2}U_{nb}^{\xi_2} + \sum_{nc} a_{nc}^{\xi_2}U_{nc}^{\xi_2} + b^{\xi_2,c} + A_{\xi_2}(p_P - p_S) + b^{\xi_2}, \tag{31}$$

$$a_b^{\xi_3}U_b^{\xi_3} = \sum_{nb} a_{nb}^{\xi_3}U_{nb}^{\xi_3} + \sum_{nc} a_{nc}^{\xi_3}U_{nc}^{\xi_3} + b^{\xi_3,c} + A_{\xi_3}(p_P - p_B) + b^{\xi_3}, \tag{32}$$

where the superscripts indicate the different coefficients associated with different velocity components, the second summation on the right-hand side includes partial non-orthogonal terms, the third term on the right-hand side is a source term due to the curvature and the last term contains non-orthogonal pressure terms.

3.3. *Discretization of the continuity equation*

Integrating the continuity equation

$$\nabla\cdot\rho\mathbf{u} = 0 \tag{33}$$

over a scalar control volume as shown in Figure 2 and applying the divergence theorem yields

$$(\rho\mathbf{u}\cdot\mathbf{S}^1)_e - (\rho\mathbf{u}\cdot\mathbf{S}^1)_w + (\rho\mathbf{u}\cdot\mathbf{S}^2)_n - (\rho\mathbf{u}\cdot\mathbf{S}^2)_s + (\rho\mathbf{u}\cdot\mathbf{S}^3)_t - (\rho\mathbf{u}\cdot\mathbf{S}^3)_b \approx \oint_{\partial V}\rho\mathbf{u}\cdot d\mathbf{S} = 0. \tag{34}$$

Substituti ıg equation (23) into the above equation yields the discretization equation

$$(c_1U^{\xi_1})_e - (c_1U^{\xi_1})_w + (c_2U^{\xi_2})_n - (c_2U^{\xi_2})_s + (c_3U^{\xi_3})_t - (c_3U^{\xi_3})_b = 0, \tag{35}$$

where

$$c_i = \rho|\mathbf{S}^i|\cos\alpha_i.$$

With this formulation the mass conservation equation is expressed exactly using the tangential velocity components without any extra source terms.

4. SOLUTION PROCEDURE

The evaluation of the pressure field has always been a difficult issue in the primitive variable approach to incompressible flow, since the pressure is indirectly involved in the continuity equation. This difficulty becomes more acute when a curvilinear co-ordinate system is used, since the expressions for the pressure gradient and the continuity equation become much more complicated. In this section a block-implicit coupled equation solver is presented. This method was first used in Reference 19 to solve two-dimensional steady incompressible flow using a Cartesian co-ordinate system and was observed to provide good convergence rates.

The pressure and velocities for a typical control volume are shown in Figure 5. The pressure located at the centre and the velocities located on the control volume surfaces are treated as the unknowns, while the pressure and velocities at all other points are treated explicitly. The momentum equations (30)–(32) provide the six algebraic equations for the six unknown velocities. These equations can be simplified by treating only two variables implicitly for each equation and written as

$$a^{\xi_1}_{p,w} U^{\xi_1}_w - A^{\xi_1}_w P_P = R_1, \tag{36}$$

$$a^{\xi_1}_{p,e} U^{\xi_1}_e + A^{\xi_1}_e P_P = R_2, \tag{37}$$

$$a^{\xi_2}_{p,s} U^{\xi_2}_s - A^{\xi_2}_s P_P = R_3, \tag{38}$$

$$a^{\xi_2}_{p,n} U^{\xi_2}_n + A^{\xi_2}_n P_P = R_4, \tag{39}$$

$$a^{\xi_3}_{p,b} U^{\xi_3}_b - A^{\xi_3}_b P_P = R_5, \tag{40}$$

$$a^{\xi_3}_{p,t} U^{\xi_3}_t + A^{\xi_3}_t P_p = R_6, \tag{41}$$

where the R_i ($i = 1, 2, \ldots, 6$) include all other terms left in the equations, calculated using the currently available values of the velocity and pressure at the neighbouring points. This approach is intended to provide a simple algebraic system which can be solved efficiently. The continuity equation (35) provides an additional algebraic equation, i.e.

$$c_{1,e} U^{\xi_1}_e - c_{1,w} U^{\xi_1}_w + c_{2,n} U^{\xi_2}_n - c_{2,s} U^{\xi_2}_s + c_{3,t} U^{\xi_3}_t - c_{3,b} U^{\xi_3}_b = 0. \tag{42}$$

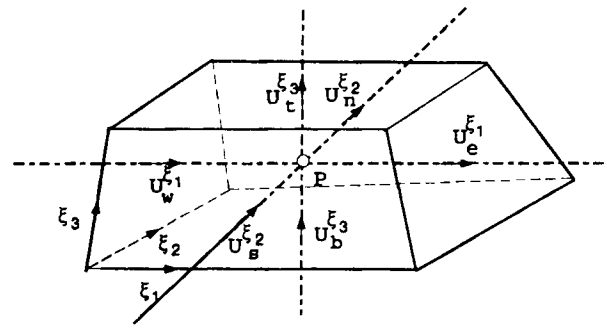

Figure 5. A general scalar control volume with seven unknowns

These equations are arranged in a block structure as

$$\begin{bmatrix} a^{\xi_1}_{p,w} & 0 & 0 & 0 & 0 & 0 & -A^{\xi_1}_{w} \\ 0 & a^{\xi_1}_{p,e} & 0 & 0 & 0 & 0 & A^{\xi_1}_{e} \\ 0 & 0 & a^{\xi_2}_{p,s} & 0 & 0 & 0 & -A^{\xi_2}_{s} \\ 0 & 0 & 0 & a^{\xi_2}_{p,n} & 0 & 0 & A^{\xi_2}_{n} \\ 0 & 0 & 0 & 0 & a^{\xi_3}_{p,b} & 0 & -A^{\xi_3}_{b} \\ 0 & 0 & 0 & 0 & 0 & a^{\xi_3}_{p,t} & A^{\xi_3}_{t} \\ c_{1,e} & -c_{1,w} & c_{2,n} & -c_{2,s} & c_{3,t} & -c_{3,b} & 0 \end{bmatrix} \times \begin{bmatrix} U^{\xi_1}_{w} \\ U^{\xi_1}_{e} \\ U^{\xi_2}_{s} \\ U^{\xi_2}_{n} \\ U^{\xi_3}_{b} \\ U^{\xi_3}_{t} \\ P_P \end{bmatrix} = \begin{bmatrix} R_1 \\ R_2 \\ R_3 \\ R_4 \\ R_5 \\ R_6 \end{bmatrix}.$$

The above block of equations is solved analytically by the Gauss elimination method. After sweeping the whole field, the coefficients $a^{\xi_i}_{nb}$, etc. are recalculated and the entire procedure is repeated until the residues become sufficiently small.

5. COMPUTATIONAL EXAMPLES

Four examples are presented in this section to demonstrate the capabilities of the proposed method using non-orthogonal grids in two- and three-dimensional geometries. All computations are carried out using the curvilinear co-ordinate-based programme CMGFD, which is based on the three-dimensional code MGFD.[20]

5.1. Cavity flow with a moving lid

The flow in a cavity with the top wall moving at a constant velocity U_w is considered. The side walls of the cavity are taken to be inclined, forming an angle β with the horizontal plane. Three cases are computed with inclinations $\beta = 60°$, 45° and 30° at a Reynolds number $Re = 100$. Calculations were performed for various grid densities and Table I lists the convergence rates for each test calculation. The convergence criterion was a maximum residual of less than 10^{-4} for each equation. The momentum residuals were normalized by ρU_w^2 and the mass residual by ρU_w. The problem was studied by Perić[13] using the Cartesian velocity unknowns in the momentum equations and a central difference scheme for the non-orthogonal terms. In contrast, the present method allows a wide range of underrelaxation factors with fast convergence for significantly non-orthogonal grids. Computational results using the finest grid, 80 × 80, are plotted in Figure 6. They show a strong main vortex driven by the lid movement and a sequence of weaker vortices in the sharp corner between the bottom plate and the upstream side wall. This second vortex system is the main difference between the square cavity and cavities with inclined walls. These results are very similar to those reported be Perić.[13]

Table I. Number of iterations necessary for convergence

Grid	20 × 20			40 × 40			80 × 80		
Inclination β	60°	45°	30°	60°	45°	30°	60°	45°	30°
Number of iterations	75	85	110	141	160	190	310	396	450

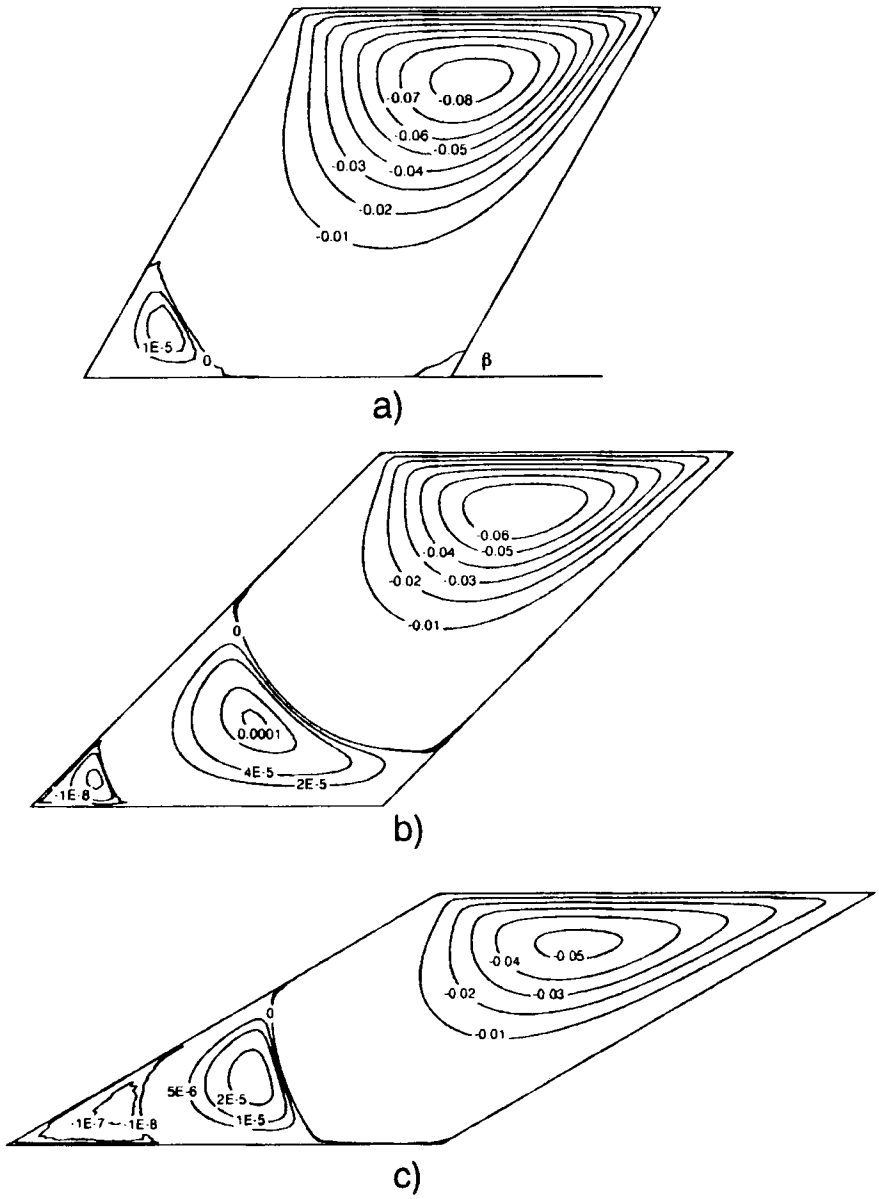

Figure 6. Streamlines for flow in cavities with inclined side wall: (a) $\beta = 60°$; (b) $\beta = 45°$; (c) $\beta = 30°$

5.2. *Laminar flow through a tube with a constriction*

As the second example, laminar flow through a tube with an axisymmetric constriction was considered. Such flows were studied experimentally by Young and Tsai.[21] The general shape of the axisymmetric constriction was specified as a cosine curve

$$\frac{R}{R_0} = 1 - \frac{\delta}{R_0} \cos\left(\frac{\pi x}{2X_0}\right), \quad -X_0 < x < X_0,$$

as shown in Figure 7(a), where the length X_0 and height δ of the constriction are parameters which can be varied for different flow situations.

The present work investigates geometries corresponding to 'Model-2' of the experimental work.[21] For this model the geometry is specified as

$$R_0 = 9{\cdot}45 \times 10^{-3}\ \text{m}, \qquad \delta/R_0 = \tfrac{2}{3}, \qquad X_0/R_0 = 4.$$

The boundary conditions imposed were no slip on the wall, zero streamwise gradient at the outlet, fully developed parabolic flow at the inlet and symmetry conditions on the axis. An 80×20 grid in the co-ordinates (x, r) was used for the calculations (see Figure 7(a)). The density of the grid points was higher near the wall and the grid was stretched in the axial direction, with more grid points in the constricted region. Computations were carried out at $Re = 50$ and 100, with the Reynolds number defined as

$$Re = 2\bar{U}R_0/\nu,$$

where $\bar{U}$ is the mean velocity of the inflow. The predicted flow field and streamlines for $Re = 50$ are plotted in Figures 7(b) and 7(c) respectively. The flow pattern for $Re = 100$ is very similar, except for the size of the recirculation zone.

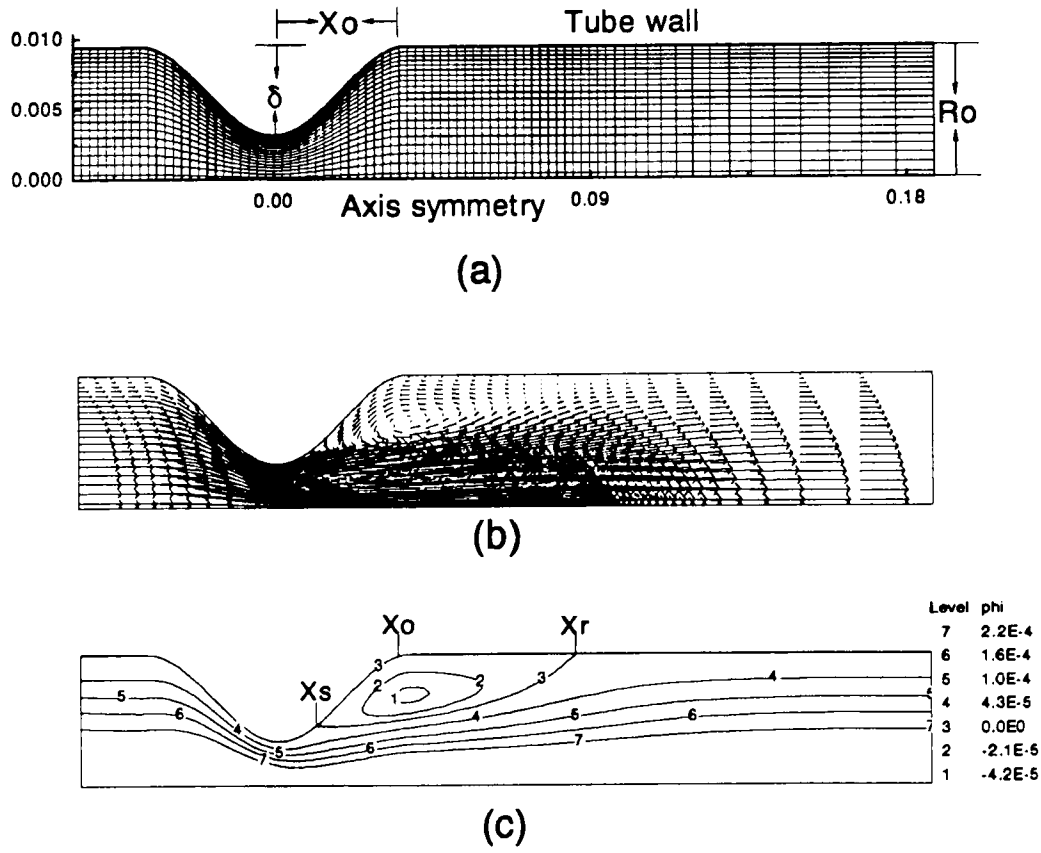

Figure 7. Flow through tube with constriction: (a) geometry and grid; (b) velocity field; (c) streamlines

The predicted separation and reattachment lengths together with experimental results from Reference 21 are presented in Table II. Excellent agreement is seen between the present computations and the experimental results.

5.3. *Developing laminar flow in a pipe*

For the third computational example, laminar flow through a pipe was considered. This flow can be considered to be two-dimensional because of axisymmetry. However, the use of a non-orthogonal grid in the present calculation makes the problem appear fully three-dimensional (see Figure 8(a)). This problem was chosen because the available analytical solution makes it possible to test the accuracy of the proposed method.

The 16×50 mesh illustrated in Figure 8(a) was generated by solving an elliptic grid generation system. The three-dimensional incompressible Navier–Stokes equations were solved with a no-slip condition at the wall, a uniform velocity profile ($w = 1$) at the inlet and zero streamwise gradient at the outlet. The pipe length was chosen as 12 times the diameter (D) for the computations and the Reynolds number was $Re_D = 100$. Using the same convergence criterion as in the previous problem, a solution was obtained after 480 iterations. Figure 8(b) shows the velocity vectors in the symmetry plane. Figure 8(c) shows the calculated velocity contour in a cross-plane located 10 diameters downstream ($x/D = 10$). Figure 8(d) compares the calculated solution in the well-developed region ($x/D = 10$) with the analytical solution $u(r) = 2(1 - r)^2$. Figure 8(e) compares the maximum velocity in the developing region with the results from Reference 22. It should be noted that the numerical solutions were obtained with the elliptic governing differential equations whereas the analytical solutions were for the parabolic forms of these equations. The results show good agreement between the analytical and numerical solutions.

5.4. *Flow in a pipe with a smooth 90° bend*

For this example, laminar flow in a pipe with a smooth 90° bend was considered. This is a strongly three-dimensional flow where the main flow in the streamwise direction along the pipe is influenced by strong secondary currents in the pipe cross-section arising from the centrifugal forces due to the bend curvature. This flow was studied experimentally by Enayet *et al.*[23] The same geometry as used in the experimental study was adopted for the present computation. The geometry and grid are illustrated in Figure 9. Owing to symmetry, the computational domain has been limited to half the pipe only. A $32 \times 32 \times 64$ mesh was used in the computations, which were carried out at $Re = \rho U_b D/\mu = 500$, corresponding to the experiment, where U_b

Table II. Comparison with experimental results and number of iterations for calculation

80×20		Separation point		Reattachment point	
Re	Number of iterations	Experiment	Prediction	Experiment	Prediction
50	210	0·33	0·32	2·28	2·27
100	241	0·34	0·33	4·19	4·10

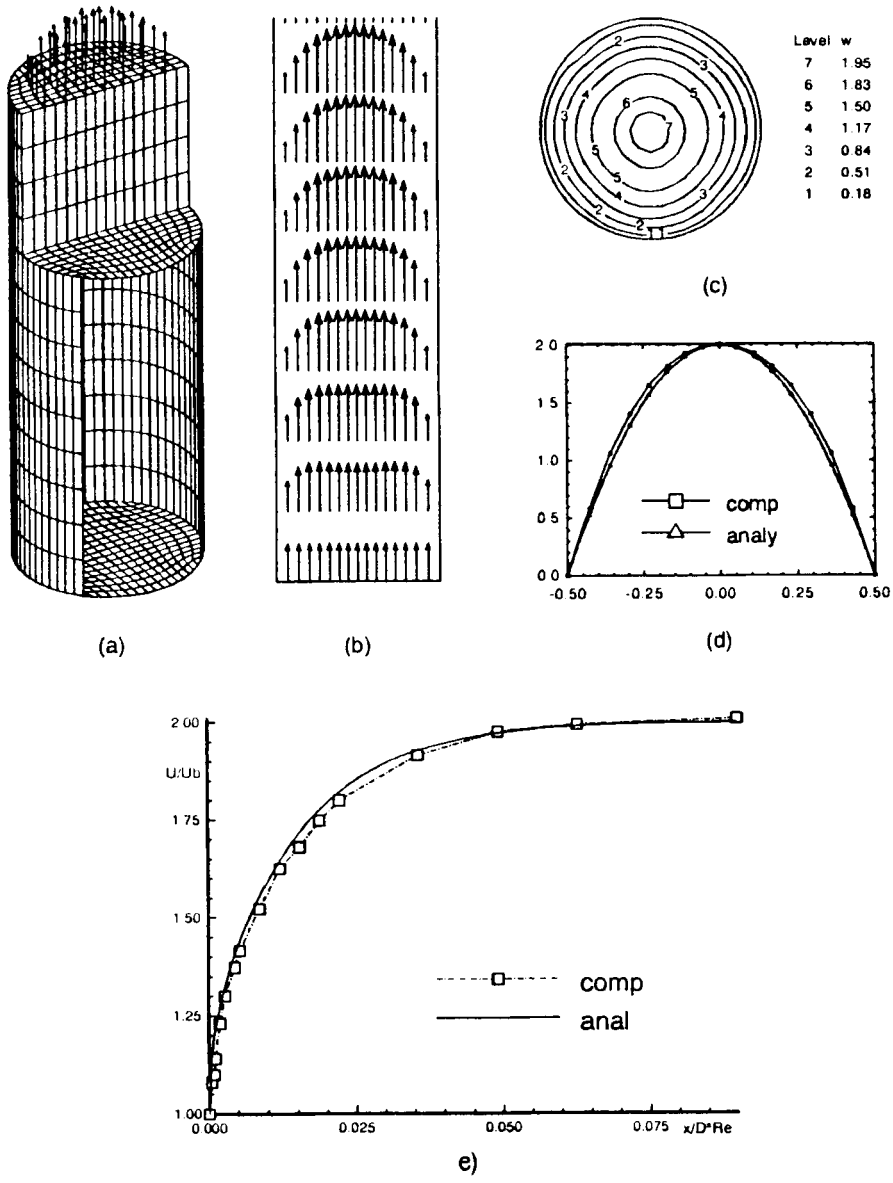

Figure 8. (a) Illustration of grid and velocity; (b) development of velocity profile; (c) velocity contour in cross-pipe plane at $x = 10D$; (d) comparison with analytic solution at $x = 10D$; (e) comparison of flow in developing region, where $U/U_b = U_{max}/U_{bulk}$

is the bulk velocity at the entrance. The convergence criterion was the same as that used in the first example, with convergence being satisfied after 620 iterations. Figure 10 shows the calculated velocity vectors in the plane of symmetry. The predicted velocities at four cross-stream locations in the plane of symmetry together with the measured results[23] are plotted in Figure 11, where reasonable agreement can be seen.

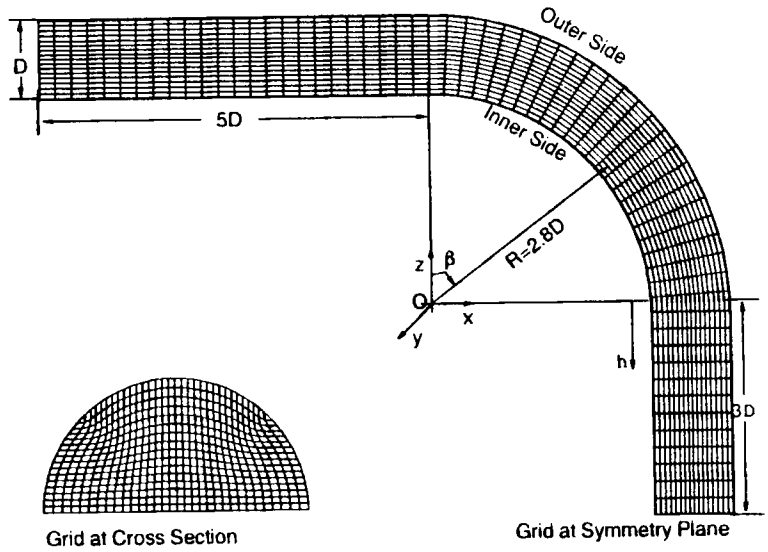

Figure 9. Grid and flow geometry for pipe with smooth 90° bend

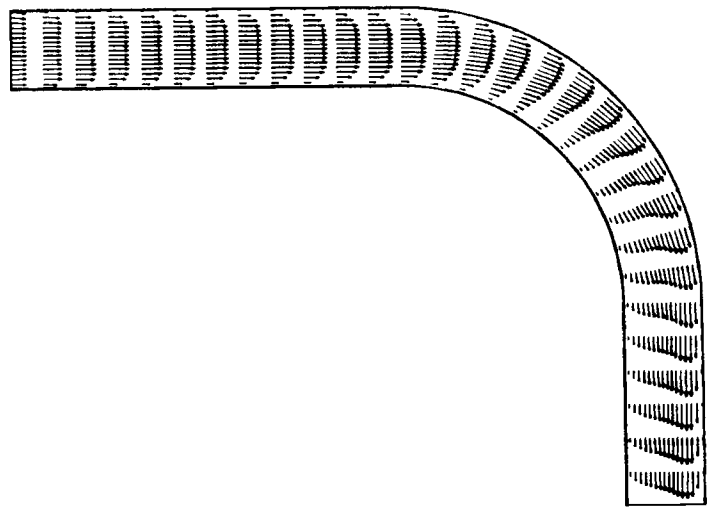

Figure 10. Velocity vectors on symmetry plane

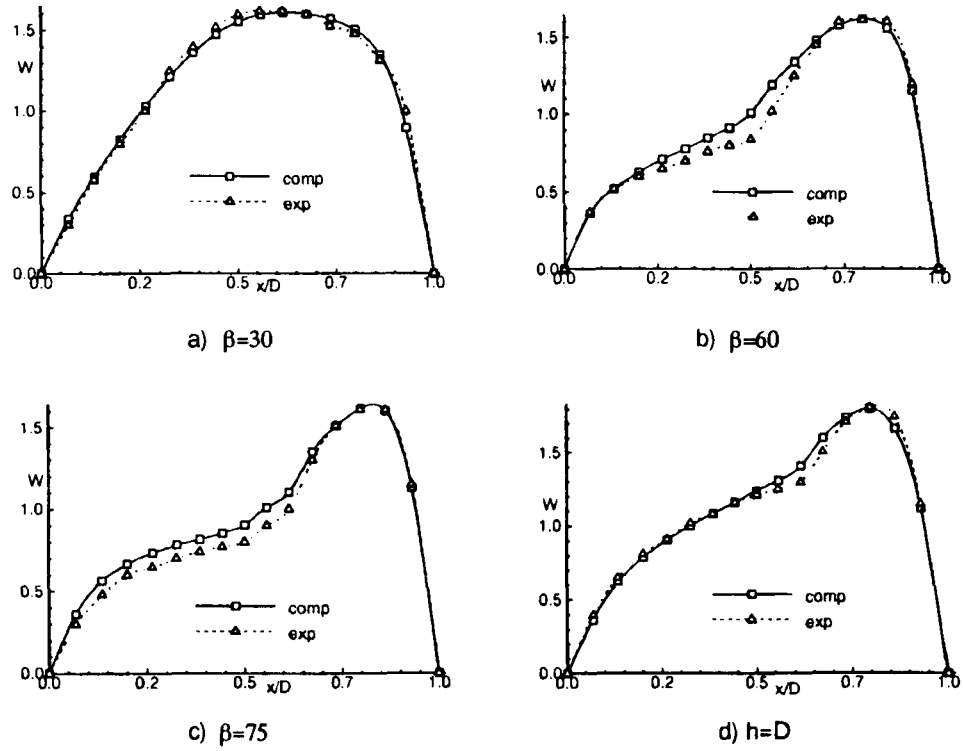

Figure 11. Comparison with experimental results

6. CONCLUSIONS

A numerical method for computing fluid flow in complex three-dimensional domains has been presented. Computational examples show that the proposed method can be used to solve flow problems in complex three-dimensional geometries using significantly non-orthogonal and moderately non-smooth grids. A new scheme for handling the non-orthogonal terms is proposed which is useful when the grid is significantly non-orthogonal.

Efforts have been made to allow for the use of moderately non-smooth grids by directly employing the geometric quantities of control cells and avoiding explicit discretization of the derivatives of the grid co-ordinates. However, the use of highly non-smooth grids should be avoided in order to obtain a reasonably accurate solution. Convergence difficulties may occur if the grids change direction rapidly from point to point. The method for dealing with the curvature terms needs to be investigated further to allow for highly non-smooth grids.

The proposed method has been implemented with a block multigrid method and further work will include implementation of a turbulence model.

ACKNOWLEDGEMENTS

The authors would like to thank Professor I. S. Gartshore, Professor B. Seymour, Dr. Z. Abdullah and Dr. P. Nowak for their contributions. Funding by the Natural Sciences and Engineering Research Council of Canada is gratefully acknowledged.

APPENDIX: NOMENCLATURE

$\mathbf{a}_i$, $\mathbf{a}^i$	covariant, contravariant vectors
a_{nb}, etc.	discretization coefficients
$\mathbf{e}_i$	unit tangent vectors (Figure 1)
$\mathbf{e}^i$	rescaled surface area vectors
F^i	volume flow rates across cell faces
g^{ij}	surface area metric tensor
$\mathbf{J}$	flow flux
p	pressure
$\mathbf{S}^i$	surface area vectors (Figure 1)
$\mathbf{u}$	velocity vector
U^i	contravariant velocities
U^{ξ_i}	tangential velocity components
V	volume of control cells

Greek letters

α_i	non-orthogonal angles, (Figure 1)
Γ	general diffusivity coefficient
ξ_i	curvilinear co-ordinates
ρ	density of fluid
ϕ	general dependent variable

Subscripts

e, w, ...	pertaining to faces of control cells
E, W, ...	pertaining to main cell centres

Superscript

ξ_i	coefficients associated with discretization for U^{ξ_i}

REFERENCES

1. M. Salcudean, I. Gartshore, K. Zhang and I. Mclean, 'An experimental study of film cooling effectiveness in the leading edge region of a turbine blade, Part I', *Tech. Rep.*, Department of Mechanical Engineering, University of British Columbia, 1991.
2. S. V. Patankar, *Numerical heat Transfer and Fluid Flow*, Hemisphere, Washington, DC, 1980.
3. C. R. Maliska and G. D. Raithby, 'A method for computing three-dimensional flows using non-orthogonal boundary-fitted coordinates', *Int. j. numer. methods fluids*, **4**, 518–537 (1984).
4. W. Shyy, S. S. Tong and S. M. Correa, 'Numerical recirculating flow calculations using a body-fitted coordinate system', *Numer. Heat Transfer*, **8**, 99–113 (1985).
5. W. Rodi, S. Majumdar and B. Schonung, 'Finite volume methods for two-dimensional incompressible flows with complex boundaries', *Comput. Methods Appl. Mech. Eng.*, **75**, 369–392 (1989).
6. L. Davidson and P. Hedberg, 'Mathematical derivation of a finite volume formulation for laminear flow in complex geometries', *Int. j. numer. methods fluids*, **9**, 531–540 (1989).
7. M. Rosenfeld, D. Kwak and M. Vinokur, 'A solution method for the unsteady incompressible navier–Stokes equations in generalized coordinate systems', *AIAA Paper 88-0718*, 1988.
8. A. Segal, P. Wesseling, J. Van Kan, C. W. Oosterlee and K. Kassels, 'Invariant discretization of the incompressible Navier–Stokes equations in boundary fitted coordinates', *Int. j. numer. methods fluids*, **15**, 411–426 (1992).
9. I. Demirdzic, A. D. Gosman, R. I. Issa and M. Perić, 'A calculation procedure for turbulent flow in complex geometries', *Comput. Fluids*, **15**, 251–173 (1987).

10. M. Faghri, E. M. Sparrow and S. T. Prata, 'Finite difference solutions of convection diffusion problems in irregular domains using nonorthogonal coordinate transformation', *Numer. Heat Transfer*, **7**, 183–209 (1984).
11. K. C. Karki and S. V. Patankar, 'Calculation procedure for viscous incompressible flows in complex geometries', *Numer. Heat Transfer*, **14**, 295–307 (1988).
12. D. Lee and J. J. Chiu, 'Covariant velocity-based calculation procedure with nonstaggered grids for computation of pulsatile flows', *Numer. Heat Transfer B*, **21**, 269–286 (1992).
13. M. Perić, 'Analysis of pressure–velocity coupling on nonorthogonal grids', *Numer. Heat Transfer B*, **17**, 63–82 (1990).
14. M. E. Braaten and W. Shyy, 'Comparison of iterative and direct solution methods for viscous flow calculations in body-fitted coordinates', *Int. j. numer. methods fluids*, **6**, 325–349 (1986).
15. M. Vinokur, 'An analysis of finite-difference and finite-volume formulations of conservation laws', *J. Comput. Phys.*, **81**, 1 (1989).
16. J. F. Thompson, Z. U. A. Warsi and C. W. Mastin, *Numerical Grid Generation, Foundations and Applications*, Elsevier, New york, 1985.
17. A. I. Brorisenko and I. E. Tarapov, *Vector and Tensor Analysis with Applications*, Prentice-Hall, Englewood Cliffs, NJ, 1968.
18. M. C. Melaaen, 'Calculation of fluid flows with staggered and nonstaggered curvilinear nonorthogonal grids—Theory', *Numer. Heat Transfer A*, **21**, 1–19 (1992).
19. S. P. Vanka, 'Block-implicit multigrid solution of Navier–Stokes equations in primitive variables', *J. Comput. Phys.*, **65**, 138–158 (1986).
20. P. Nowak, 'MGFD: a general three-dimensional multigrid code', *Tech. Rep.*, Department of Mechanical Engineering, University of British Columbia, 1992.
21. D. F. Young and F. Y. Tsai, 'Flow characteristics in models of arterial stenoses—I. Steady flow', *J. Biomech.*, **6**, 395–410 (1973).
22. R. K. Shah and A. L. London, *Advances in Heat Transfer*, Suppl. 1, Academic, New York, 1978.
23. M. M. Enayet, M. M. Gibson, A. M. K. P. Taylor and M. Yianneskis, 'Laser-doppler measurements of laminar and turbulent flow in a pipe bend', *Int. J. Heat Fluid Flow*, **3**, 213–219 (1982).